Geothermics 101 (2022) 102351



Contents lists available at ScienceDirect

Geothermics

journal homepage: www.elsevier.com/locate/geothermics

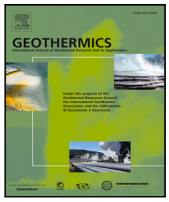



Ground heat exchange potential of Green Infrastructure

Anil Yildiz [a,b,c], Ross A. Stirling [b,c,*]

[a] Methods for Model-based Development in Computational Engineering, RWTH Aachen University, Aachen, 52062, Germany
[b] School of Engineering, Newcastle University, Newcastle upon Tyne, NE1 7RU, United Kingdom
[c] National Green Infrastructure Facility, Newcastle University, Newcastle upon Tyne, NE4 5TG, United Kingdom

ARTICLE INFO

Keywords:
Green infrastructure
Ground heat exchangers
Heat injection
Field testing
Numerical modelling

ABSTRACT

Both Green Infrastructure and Ground Source Heat Exchangers provide opportunities to significantly improve the resilience and sustainability of our built environment. This work explores the thermo-hydrological response of a vegetated Sustainable Drainage System under physically simulated heat injection conditions using a soil column of 1800 mm diameter and 950 mm height in a heavily-instrumented lysimeter. A range of field testing scenarios (thermal load and cycling) were applied under natural, external ambient conditions. Soil temperature during heat injection was also simulated numerically by solving a transient heat conduction equation with a finite difference modelling scheme. The developed model was validated using measurements from the lysimeter setup which then enabled numerical experiments into the effects of varying hydrological regimes to be performed. Results of the field testing showed that heat injection propagates a temperature change only at deeper layers, while the temperature of shallow layers are still governed by the atmospheric conditions.

1. Introduction

Energy demand for space heating and cooling accounts for nearly a third of the final energy demand in the 28 member states of the European Union, the majority of which comes from residential buildings, supplied with energy generated from fossil fuels (Fleiter et al., 2017). The inevitable need to reduce fossil fuel consumption has led to an increased need to rapidly develop renewable energy solutions, including the use of multiple sources.

Geothermal energy, which has been documented to be utilised in more than 80 countries (Lund and Boyd, 2016), is an alternative to fossil fuels for electricity generation, direct heating, and indirect heating and cooling via ground source heat pumps (GSHP) (Self et al., 2013). GSHP systems consist of a heat pump, a heat exchanger fluid and a ground heat exchanger in which the fluid is circulated. The coefficient of performance of GSHP systems is higher than conventional systems (Healy and Ugursal, 1997), and their market share is expected to increase in the United Kingdom (Day et al., 2009).

The most commonly used type of ground heat exchangers is the closed loop vertical GHEs within boreholes (Go et al., 2015), however drilling deep boreholes results in a budget that might be excessive for small residential and commercial applications. Horizontal GHEs buried in shallow trenches offer a viable alternative solution for smaller demands, as trench installation requires a lower budget (Wu et al., 2015), however a large area of land is needed (Go et al., 2015). The implementation of shallow GHEs in rural areas are relatively easier compared to urban areas due to the vast amounts of available land (Šeďová et al., 2013). Dedicating areas to build shallow GHEs in urban areas is even more problematic in densely populated countries. Therefore, optimisation of pipe length is essential to minimise both the material and installation costs (Fujii et al., 2012).

The following parameters affect the performance of either deep or shallow GSHP systems, and in turn define the design criteria (Healy and Ugursal, 1997) :

- GSHP capacity
- Content and flow rate of heat transfer fluid
- Type of GHE
- Depth, dimensioning and pipe size of GHE
- Soil thermal properties

The first four items in this list can increase the efficiency or performance of a GSHP system if one invests in more material or advanced technology, which may not always be cost-effective. For example, GHE type, e.g. horizontal slinky or coil, can be much more influential for shallow GHEs than the pipe diameter (Kim et al., 2016). However, accurate estimation of mean thermal properties is among the most important design constraints of GSHP systems (Simms et al., 2014), and varying soil thermal properties, e.g. thermal conductivity, determine

* Corresponding author at: School of Engineering, Newcastle University, Newcastle upon Tyne, NE1 7RU, United Kingdom.
E-mail address: ross.stirling@newcastle.ac.uk (R.A. Stirling).

https://doi.org/10.1016/j.geothermics.2022.102351
Received 5 September 2021; Received in revised form 21 December 2021; Accepted 12 January 2022
Available online 5 February 2022
0375-6505/© 2022 The Authors. Published by Elsevier Ltd. This is an open access article under the CC BY license (http://creativecommons.org/licenses/by/4.0/).

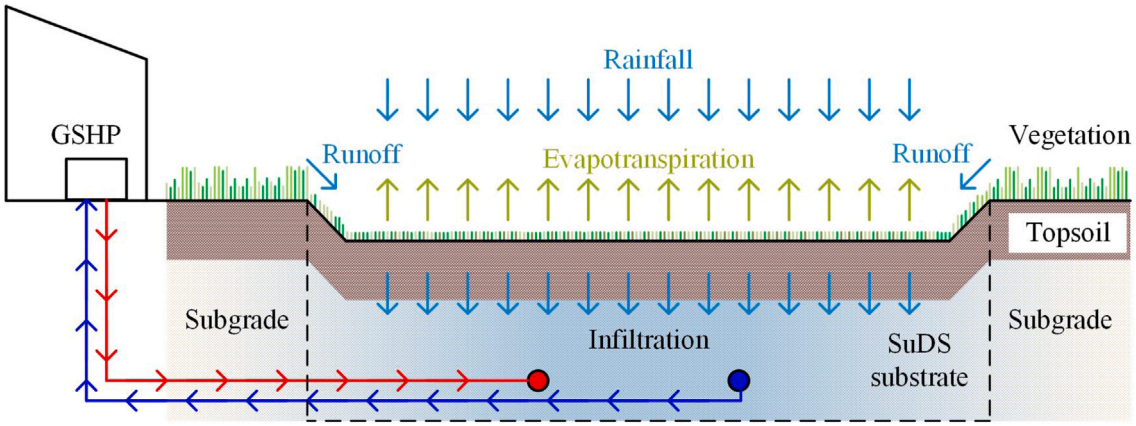

Fig. 1. Conceptual illustration of combining Sustainable Drainage Systems (SuDS) with a Ground Source Heat Pump (GSHP) system.

the thermal exchange capacity, and, in turn, will affect the performance of the system significantly (Dalla Santa et al., 2020).

Numerous evidences are available in the literature documenting the relationship between the thermal efficiency of the system and the thermal conductivity of the medium (Chong et al., 2013; Naylor et al., 2015; Wu et al., 2015). Bulk thermal conductivity for soils is a function of mineralogy, density and water content (De Vries, 1963). As shallow GHEs are built in trenches with compacted backfill materials, the variation mostly comes from changes in the water content (Wu et al., 2015). Groundwater flow for deep GHEs (Hwang et al., 2010) and rainfall infiltration for shallow GHEs (Go et al., 2015) are found to affect the energy transfer.

Means of increasing the water content of trenches artificially have been proposed, such as directing roof drainage into the ground (Di Sipio and Bertermann, 2017), irrigating trench areas (Naylor et al., 2015; DiCarlo, 2021), and utilising rain gardens and rainwater harvesting systems (Gao et al., 2016). Sustainable Drainage Systems (SuDS) are engineered features of typically urban environments which are used primarily to manage excess surface water (e.g. road and pavement runoff). Their function is to collect, convey and attenuate the flow of water in a more sustainable and resilient manner than the more traditional "grey infrastructure" of storm drains, culverts and tanks. SuDS use nature-based processes such as infiltration to attenuate flow and vegetation for filtration and restoration of water storage capacity via root-water uptake and transpiration. Other engineering benefits of SuDS include their contribution to improved water quality (López et al., 2020), air quality (Kumar et al., 2019), and reduction of urban heat island effects (Marando et al., 2022). The multi-beneficial nature of SuDS can be exploited in terms of serving as a medium for shallow GHEs, as they are purpose-built to hold water in their substrates. However, the co-location of GHE and SuDS is not documented as common practice. Fig. 1 illustrates the concept proposed to combine SuDS with shallow GHEs in urban settings.

Green infrastructure (GI), in the form of green roofs and living walls, has been used mostly as a means of passive cooling (de Gracia et al., 2018), but the potential of other components of GI needs to be investigated. There is a bifold benefit in utilising SuDS in GSHP application in urban areas. Firstly, it removes the need to dedicate space to build shallow GHEs. Secondly, the substrate of SuDS can remain in the high thermal conductivity range, even in Summer (Yildiz and Stirling, 2021c), which is similar to the design values suggested by Dalla Santa et al. (2020). This highly conductive substrate can increase the efficiency of the GSHP system.

This study aims to present the behaviour of simulated, both physically and numerically, heat injection into a purpose-built at-scale GI component. The objectives are to investigate the temperature fluctuation in the substrate of SuDS under various heat injection thermal loading scenarios, to analyse the hydrological regime of the SuDS during heat injection, to simulate the variations in the soil temperature due to heat injection, and to perform predictions under different hydrological scenarios.

2. Field testing

2.1. Outdoor test setup

An outdoor lysimeter setup was commissioned at the National Green Infrastructure Facility in Newcastle-upon-Tyne, UK to simulate heat injection into the substrate of a bioretention cell. Fig. 2 presents the cross-section of the lysimeter, showing the soil column and the instrumentation.

The lysimeter body, made out of stainless steel, is a 2000-mm diameter cylinder with a conical bottom fitted with a flow gauge to measure the water drained. The depth of the lysimeter is 1100 mm at the edges, whereas it is 1200 mm at the centre. The bottom of the lysimeter was filled with gravel until a clear height of 1000 mm was reached, which is topped with a non-woven geotextile to prevent migration of fine particles.

A high density polyethylene (HDPE) pipe with an inner diameter of 1800 mm and a wall thickness of 80 mm was placed above the gravel layer to prevent the direct contact of the soil column with the steel body and to reduce the effects of external atmospheric conditions. The pipe wall comprised a helical air void approximately 64 mm thick between two 8 mm HDPE walls. Given the significantly lower thermal conductivity of air (0.026 W/m K at 16 °C and 100 kPa atmospheric pressure) compared to the steel lysimeter lining (14.4 W/m K — stainless steel 304), this layer is considered as thermal insulator to the soil column. A weather station, a rainfall gauge and a net radiometer are placed immediately above to obtain meteorological parameters, such as air temperature, rainfall, net radiation, relative humidity and wind speed.

2.2. Preparation of the soil column

A 950-mm-high soil column was built in the lysimeter using a 800-mm-thick fine sand layer and a 150-mm-thick topsoil layer similar to a bioretention cell. Table 1 presents the basic properties of the soils used. Optimum water content of the sand, i.e. 16%, was chosen as a target value at a relative density of 35% – which corresponds to a bulk density of 1.68 Mg/m^3. Sand was compacted as 100-mm thick layers with a 6-kg compaction hammer. Core-cutter density measurements taken after compaction yielded an average bulk density of 1.67 Mg/m^3 and a gravimetric water content of 16.6%. A total of 460 kg of topsoil was placed above the sand as a 150-mm thick layer, which gives an overall bulk density of 1.20 Mg/m^3. Topsoil was sown with winter grazing ryegrass seeds (*Secale cereale*). Details of the preparation of the soil column can be found in Yildiz and Stirling (2021c).

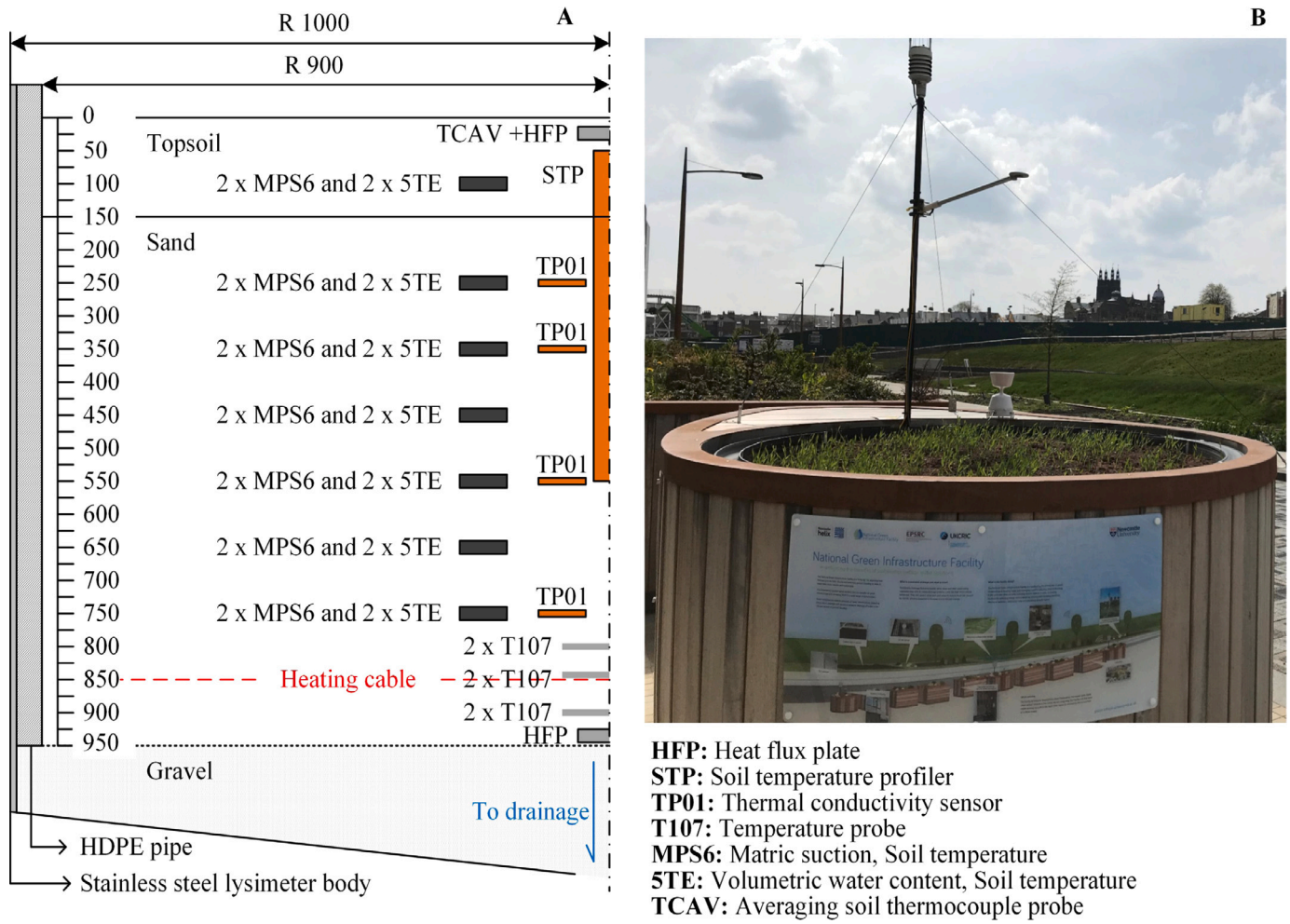

Fig. 2. (A) Axisymmetric cross-section of the lysimeter setup showing the soil column and the instrumentation. Units are given in millimetres. (B) A photograph taken 2 weeks after the commissioning showing the setup as well as the weather station.

Table 1
Properties of the soils used in this study.

	Unit	Topsoil	Sand
Gravel	[%]	3.3	–
Sand	[%]	86.3	99.0
Fines	[%]	10.4	1.0
Specific gravity, G_s	[–]	2.41	2.68
Mean particle size, d_50	[mm]	0.20	0.20
Coefficient of curvature, C_c	[–]	1.40	1.20
Coefficient of uniformity, C_u	[–]	3.88	2.40

2.3. Instrumentation

Fig. 2 illustrates the layout and exact location of instrumentation in the soil column. Parameters measured can be categorised as hydrological and thermal. Volumetric water content and matric suction, i.e. hydrological parameters, are measured with Decagon 5TE (Decagon Devices, Inc., 2016) and MPS6 sensors (Decagon Devices, Inc., 2017), respectively. Soil temperature, heat flux, and thermal conductivity are the thermal parameters measured. Two heat flux plates, HFP01 from Hukseflux (2021a), are placed 80 mm and 940 mm below the surface. The upper heat flux plate, in combination with a temperature averaging probe (TCAV) (Campbell Scientific, 2021c), is used to estimate the incoming flux due to solar radiation, whereas the lower one monitors the heat flux induced by the heating cable.

Soil temperature is measured with a combination of sensors. Campbell Scientific 107 (Campbell Scientific, 2021a) temperature probes are used in the vicinity of the heating cable. Two sensors of each are placed at 800 mm, immediately above the heating cable at 850 mm and at 900 mm depth. MPS6 and 5TE sensors, at 100 mm below the surface in the topsoil and at every 100 mm starting from 250 mm up to 750 mm in the sand, provide temperature readings in addition to their own functions. A temperature profiler, STP01 from Hukseflux (2021b), provides measurements at 70, 100, 150, 250 and 550 mm. Lastly, thermal conductivity is measured at 250, 350, 550 and 750 mm with TP01 from Hukseflux (2021). Hydrological parameters are recorded with a GP2 data logger from Delta-T Devices (2021), whereas the other sensors are logged with a CR800 from Campbell Scientific (2021b).

2.4. Heat injection tests

Heat injection into the soil has been simulated using two 10-m long heating cables (BioGreen HK 10.0) to form a circle with an area of 2 m^2 at 850 mm below the surface. Cables were connected in parallel to a variable power supply. The resistance of each heating cable was measured as 540 Ω with a multimeter, while the equivalent resistance at the connection terminal to the power supply was 272.1 Ω.

Two sets of heat injection tests were performed, and the details are given in Table 2. Set I, starts at 19.07.2019 08:30 UTC and consists of three experiments, each lasting 72 h, with 96 h gaps in between. Voltage inputs were 165.6, 128.3 and 74.1 V, resulting in power inputs of 50, 30 and 10 W. The second one, Set II, consists of a total of 24 daily experiments, i.e. on between 08.00 and 16.00, off otherwise. Power input was fixed at 30 W.

Table 2
Summary of heat injection tests conducted in this study.

Set	Test	Power [W]	Start [UTC]	End [UTC]
I	1	50	2019-07-19 08:30	2019-07-22 08:30
I	2	30	2019-07-26 08:30	2019-07-29 08:30
I	3	10	2019-08-02 08:30	2019-08-05 08:30
II	1	30	2019-08-08 08:00	2019-08-08 16:00
II	2	30	2019-08-09 08:00	2019-08-09 16:00
II	3	30	2019-08-10 08:00	2019-08-10 16:00
II	4	30	2019-08-13 09:30	2019-08-13 15:45
II	5	30	2019-08-14 08:00	2019-08-14 16:00
II	6	30	2019-08-15 08:00	2019-08-15 16:00
II	7	30	2019-08-16 08:00	2019-08-16 16:00
II	8	30	2019-08-19 08:00	2019-08-19 16:00
II	9	30	2019-08-20 08:00	2019-08-20 16:00
II	10	30	2019-08-21 08:00	2019-08-21 16:00
II	11	30	2019-08-22 08:00	2019-08-22 16:00
II	12	30	2019-08-28 08:00	2019-08-28 16:00
II	13	30	2019-08-29 08:00	2019-08-29 16:00
II	14	30	2019-08-30 08:00	2019-08-30 16:00
II	15	30	2019-08-31 08:00	2019-08-31 16:00
II	16	30	2019-09-01 08:00	2019-09-01 16:00
II	17	30	2019-09-02 08:00	2019-09-02 16:00
II	18	30	2019-09-03 08:00	2019-09-03 16:00
II	19	30	2019-09-04 08:00	2019-09-04 16:00
II	20	30	2019-09-05 08:00	2019-09-05 16:00
II	21	30	2019-09-06 08:00	2019-09-06 16:00
II	22	30	2019-09-09 08:00	2019-09-09 16:00
II	23	30	2019-09-10 08:00	2019-09-10 16:00
II	24	30	2019-09-11 08:00	2019-09-11 16:00

3. Numerical modelling

3.1. Methods

The temperature variation in the soil column due to heat injection was modelled as a one-dimensional problem, as all measurements are concentrated towards the central axis. Eq. (1) shows the general form of the transient heat conduction, in which T is temperature, t is time, and α is the thermal diffusivity.

$$\frac{\partial T}{\partial t} = \nabla \alpha \nabla T \tag{1}$$

Eq. (1) can be re-written as:

$$\frac{\partial T}{\partial t} = \frac{\partial}{\partial z}\left(\alpha \frac{\partial T}{\partial z}\right) \tag{2}$$

Assuming that α changes over time and space, Eq. (2) leads to:

$$\frac{\partial T}{\partial t} = \alpha \frac{\partial^2 T}{\partial z^2} + \frac{\partial \alpha}{\partial z}\frac{\partial T}{\partial z} \tag{3}$$

Eq. (3), as the governing equation of the system, can be solved with an explicit finite difference modelling framework to obtain the change in temperature (T) in time (t). This framework helps to estimate the soil temperature at a node in the next time step, ${T_i}^{j+1}$, using the information from the previous time step $t_0 = j$. Approximating Eq. (3) with a central differencing scheme and re-arranging the terms yields ${T_i}^{j+1}$, as shown in Eq. (4).

$${T_i}^{j+1} = {T_i}^{j} + {\alpha_i}^{j}\frac{{T_{i+1}}^{j} - 2{T_i}^{j} + {T_{i-1}}^{j}}{(\Delta z)^2}\Delta t + \frac{{\alpha_{i+1}}^{j} - {\alpha_{i-1}}^{j}}{2\Delta z}\frac{{T_{i+1}}^{j} - {T_{i-1}}^{j}}{2\Delta z}\Delta t \tag{4}$$

Fig. 3 illustrates the discretisation of the soil column. In order to maintain equal node spacing, denoted as Δz, and to be able to make direct use of the field measurements for validation, the soil column was discretised such that the upper boundary is 50 mm, and the lower boundary is 850 mm. Node spacing in the upcoming equations, is taken as 50 mm. A time step, Δt, of 15 min was chosen to satisfy the Courant–Friedrichs–Levy criterion of numerical stability.

As there are no point measurements of temperature at the upper boundary at 50 mm, a linear interpolation was made between the measurements with TCAV (~40 mm) and the first measurement point

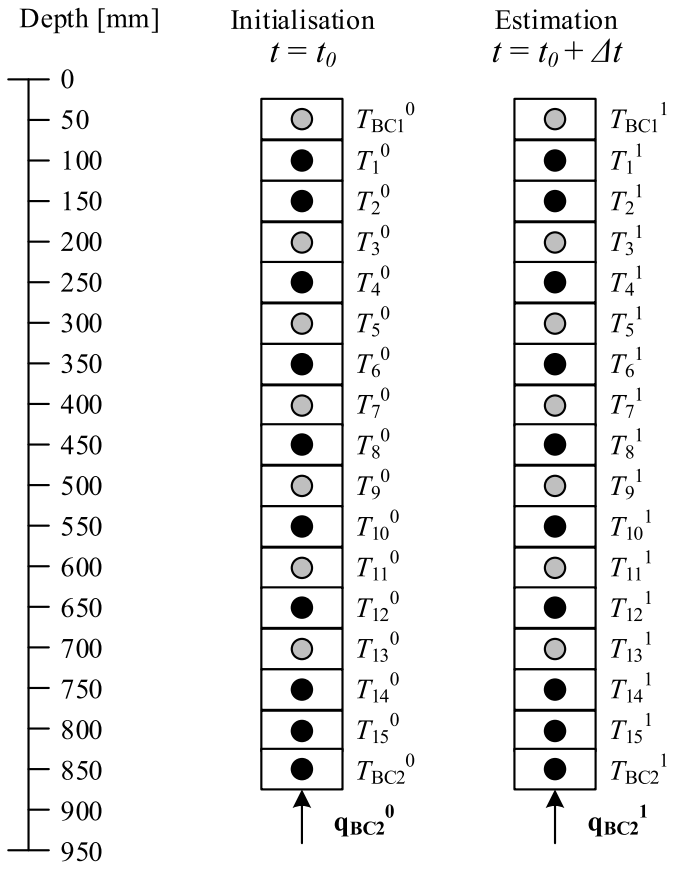

Fig. 3. Discretisation of the soil column for finite difference modelling. Black-coloured nodes show the initial conditions taken from the field measurements, while grey-coloured nodes are obtained by linear interpolation between the two closest measurement points.

of STP-01 at 70 mm (see Fig. 2), the interpolated value was taken as the prescribed temperature boundary condition, $T_{BC1}(t)$. The lower boundary condition is defined as a heat flux at the heating cable, $q_{BC2}(t)$. Heat flux at the bottom of the soil column was measured at 940 mm, $q_{940}(t)$. Therefore, the energy stored between 850 mm and 940 mm, ΔS, should be added to the flux measurements to estimate the heat flux at the boundary. Energy stored in the layer can be calculated with Eq. (5) (Ochsner et al., 2007).

$$\Delta S = \int_{z=850}^{z=940} C\frac{\partial T}{\partial t}dz + \int_{z=850}^{z=940} T\frac{\partial C}{\partial t}dz \tag{5}$$

The heat flux at the lower boundary (q_{BC2}) can be calculated as shown in Eq. (6) with the heat flux measurements (q_{940}) and the approximation of Eq. (5) with average volumetric heat capacity (C) and temperature between 850 and 940 mm, and the vertical distance between these points (d).

$$q_{BC2} = q_{940} + C^j\frac{T^{j+1} - T^j}{\Delta t}d + T^j\frac{C^{j+1} - C^j}{\Delta t}d \tag{6}$$

$${T_{BC2}}^{j+1} = {T_{BC2}}^{j} + {\alpha_{BC2}}^{j}\frac{{T_{900}}^{j} - 2{T_{BC2}}^{j} + {T_{800}}^{j}}{(\Delta z)^2}\Delta t + \frac{{\alpha_{900}}^{j} - {\alpha_{800}}^{j}}{2\Delta z}\frac{{T_{900}}^{j} - {T_{800}}^{j}}{2\Delta z}\Delta t + \frac{{q_{BC2}}^{j}\Delta t}{{C_{BC2}}^{j}\Delta z} \tag{7}$$

The temperature at the lower boundary at each time step, ${T_{BC2}}^{j+1}$, can be estimated by adding the heat generation term to Eq. (3) and re-writing it using central differencing, as shown in Eq. (7). The temperature of a node outside the calculation domain is needed to solve

this equation, which is taken as the soil temperature measurement at 900 mm (T_{900}).

Eqs. (4), (6) and (7) require the thermal properties of the soil. As the hydrological regime of the soil is fluctuating throughout the field testing period, a relationship between the volumetric water content (θ) and the thermal property in question is needed. Yildiz and Stirling (2020) presents simultaneous measurements of α (in mm^2/s) and C (in Wh/m^3 K) as a function of volumetric water content on samples prepared at the same dry density as the sand and topsoil used in the field setup. A modified sigmoid (Yildiz, 2020) and a standard sigmoid curve were fitted to the measured data in Yildiz and Stirling (2020), which are used in this study to calculate the thermal properties at each time step based on measurements of the volumetric water content from the soil column. Eqs. (8)–(10) show the aforementioned relationships for sand and topsoil. If there are no measurements at a node or a boundary, an interpolation is performed between the two closest measurement points. The result is taken as the value of the volumetric water content.

$$\alpha_{\text{sand}} = 0.25 + \frac{0.64}{1 + e^{-1.72(\theta - 6.01)}} \tag{8}$$

$$\alpha_{\text{topsoil}} = 0.23 + \frac{0.25}{1 + e^{-0.78(\theta - 11.3)}} \tag{9}$$

$$C_{\text{sand}} = 296.4 + \frac{52.7 + 8.32(\theta - 5.27)}{1 + e^{-3.24(\theta - 5.27)}} \tag{10}$$

Sigmoid function defined for α of the sand, Eq. (8), reaches to a peak value at around 8% water content, and stays constant thereafter. Closest measurement of θ to the heating cable is located at 750 mm, and the water content at that point has not dropped below approximately 12%. Therefore, change in α is negligible around the heating cable, which simplifies Eqs. (7) to (11).

$${T_{\text{BC2}}}^{j+1} = {T_{\text{BC2}}}^{j} + {\alpha_{\text{BC2}}}^{j} \frac{{T_{900}}^{j} - 2{T_{\text{BC2}}}^{j} + {T_{800}}^{j}}{(\Delta z)^2} \Delta t + \frac{{q_{\text{BC2}}}^{j} \Delta t}{{C_{\text{BC2}}}^{j} \Delta z} \tag{11}$$

Once the temperature at the lower boundary is estimated and the one at the upper boundary is taken from the interpolation, temperature at intermediate nodes ($i = 1, 2, \ldots, 15$) can be calculated using Eq. (4). Model calculations were performed in R.4.0.2 (R Core Team, 2020). R scripts used in this study for the numerical modelling can be accessed from Yildiz and Stirling (2022b). A reproducible version of this modelling scheme is presented as a Jupyter notebook (Yildiz and Stirling, 2022c). The algorithm can be summarised as follows :

Algorithm 1: Estimating soil temperature

1. Import soil temperature data at $t = t_0$ at the nodes and boundaries
2. Perform linear interpolation for nodes which do not have a measurement point
3. Calculate the thermal properties using Eqs. (8)–(10) and volumetric water content
4. Calculate the heat flux at the lower boundary using Eq. (6)
5. Estimate the soil temperature at the lower boundary at $t = t_0 + \Delta t$ using Eq. (11)
6. Calculate soil temperature at nodes at $t = t_0 + \Delta t$ using Eq. (4)
7. Initialise the next step ($t = t_0 + 2\Delta t$) with the values from Step 4 and Step 5
8. Repeat from Step 4 to Step 6.

3.2. Numerical experiments

In addition to simulation of measured conditions, numerical experiments were performed using the developed framework in order to investigate temperature fluctuations due to heat injection under different hydrological regimes. Experiments were performed using consistent boundary conditions and varying the volumetric water content at all depths. Variation of the volumetric water content results in a difference in modelled thermal properties. Numerical experiments based on Set I heat injection tests were conducted by multiplying the measured volumetric water content data at Step 3 of Algorithm 1 with the multiplication factors, k, 1.50 and 2.00.

Table 3
Summary of monthly meteorological parameters.

	Unit	July	August	September
Air temperature				
Mean value	[°C]	17.1	16.5	13.4
Exceedance probability	[%]	2.90	5.80	18.1
Return period	[years]	34.5	17.3	5.6
Rainfall				
Total value	[mm]	71.6	102.2	78.0
Exceedance probability	[%]	43.8	18.1	35.6
Return period	[years]	2.3	5.6	2.8
Relative humidity	[%]	70.8	71.4	72.3
Net radiation	[W/m^2]	47.7	32.9	6.93
Wind speed	[m/s]	1.93	2.31	2.07
Barometric pressure	[hPa]	1006	1002	1006

4. Results

4.1. Field testing

Field data presented, unless stated otherwise, cover a period from 18.07.2019 00:00 and 12.09.2019 00:00. All times herein are given in Universal Coordinated Time (UTC). Data collected in this period have been made available for public access in Yildiz and Stirling (2022a).

4.1.1. Meteorological parameters

Daily rainfall, air temperature, relative humidity and net radiation during 56 days of monitoring in the aforementioned time frame is illustrated in Fig. 4. Rainfall, i.e. more than 0.2 mm, was recorded for 21 days out of 56. Total rainfall was measured as 154.8 mm, with a maximum daily value of 37.4 mm. Air temperature and relative humidity ranged between 5.4–29.1 °C and 29.6–90.8%, respectively. A decrease in daily mean values of both air temperature and net radiation over time can also be seen in Fig. 4a and b.

Table 3 summarises the mean parameters for July, August, and September 2019. Data presented in Fig. 4 are between 18.07.2019 and 12.09.2019, however the mean values were calculated for the full duration of the corresponding calendar month. Exceedance probabilities and return periods of mean air temperature and monthly rainfall are calculated using the historical datasets from North and North East of UK dating back to 1884 for air temperature and to 1862 for rainfall (The Met Office, 2020). These three months are typical in terms of rainfall, but July 2019 has an exceptionally high air temperature with an exceedance probability of 2.9%.

4.1.2. Thermo-hydrological parameters

Fig. 5 presents the volumetric water content and thermal conductivity measurements at four locations in the soil column, as well as the rainfall and potential evapotranspiration, calculated according to FAO-56 method (Allen et al., 1998), to estimate the water balance. An initial drying phase can be seen with a minimal change in the shallow depths of sand (see Fig. 5b and c) and a reduction at deeper layers (see Fig. 5d and e). This steady change was interrupted with the rainfall between 09.08.2019 and 11.08.2019, after which the water content increases at all depths. The increase occurs more abruptly at shallow depths, whereas the volumetric water content increases less at a slower rate at deeper layers. The period after these three consecutive days with rainfall does not show any increase in water content in the sand. Thermal conductivity at all depths follow the same trend of the water content. An overall increase of thermal conductivity and volumetric water content with increasing depth can be seen in Fig. 5b–e.

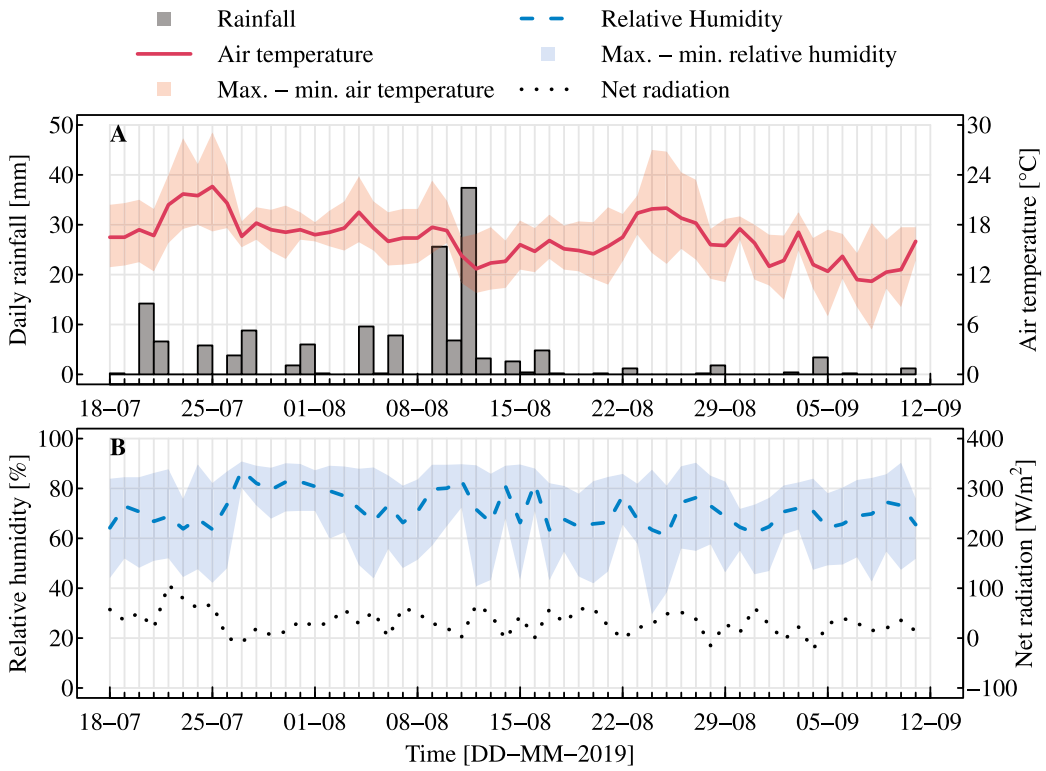

Fig. 4. (A) Daily rainfall and air temperature, as well as (B) relative humidity and net radiation during the period of monitoring. Shaded zones in each figure show the range of minimum and maximum values in a day.

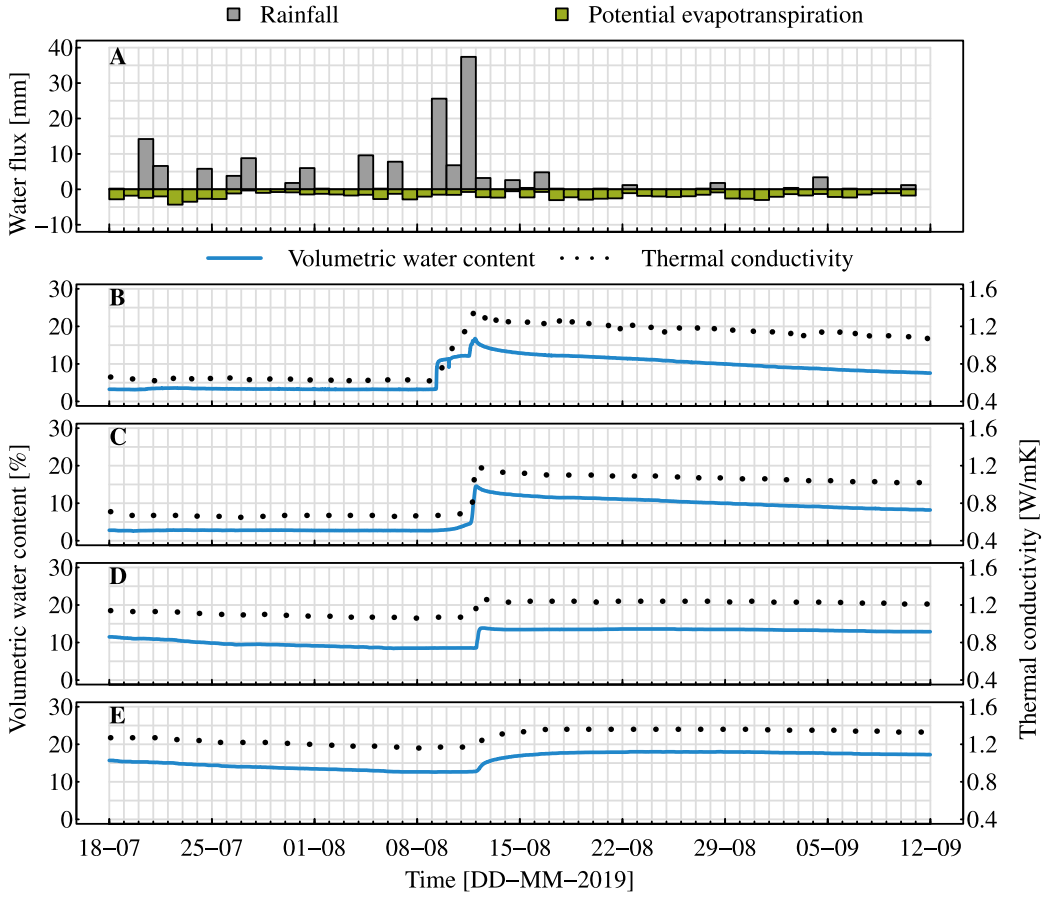

Fig. 5. (A) Water flux to and from the soil column, and volumetric water content — thermal conductivity measurements in the sand at (B) 250 mm, (C) 350 mm, (D) 550 mm and (E) 750 mm below the surface. Negative values in (A) indicate water leaving the soil column.

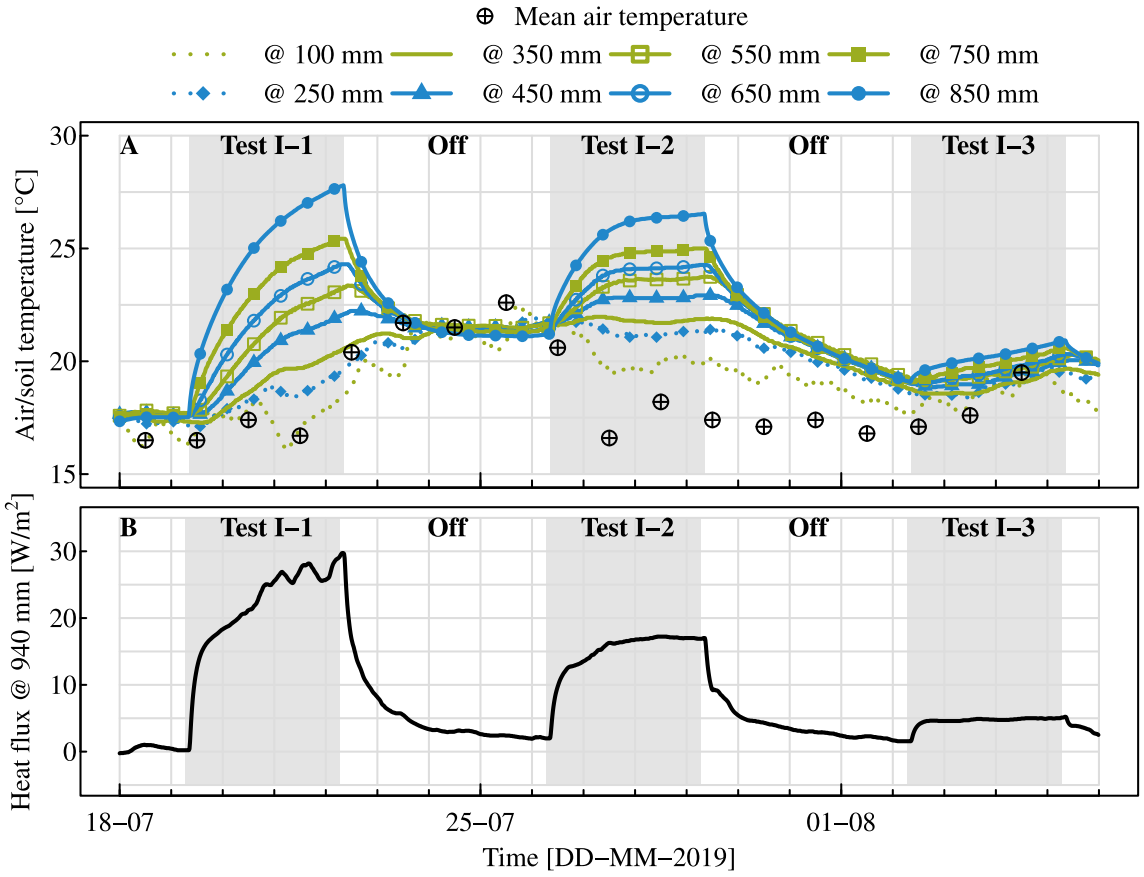

Fig. 6. (A) Air and soil temperature, as well as (B) heat flux at the bottom of the soil column during the first set of heat rejection tests.

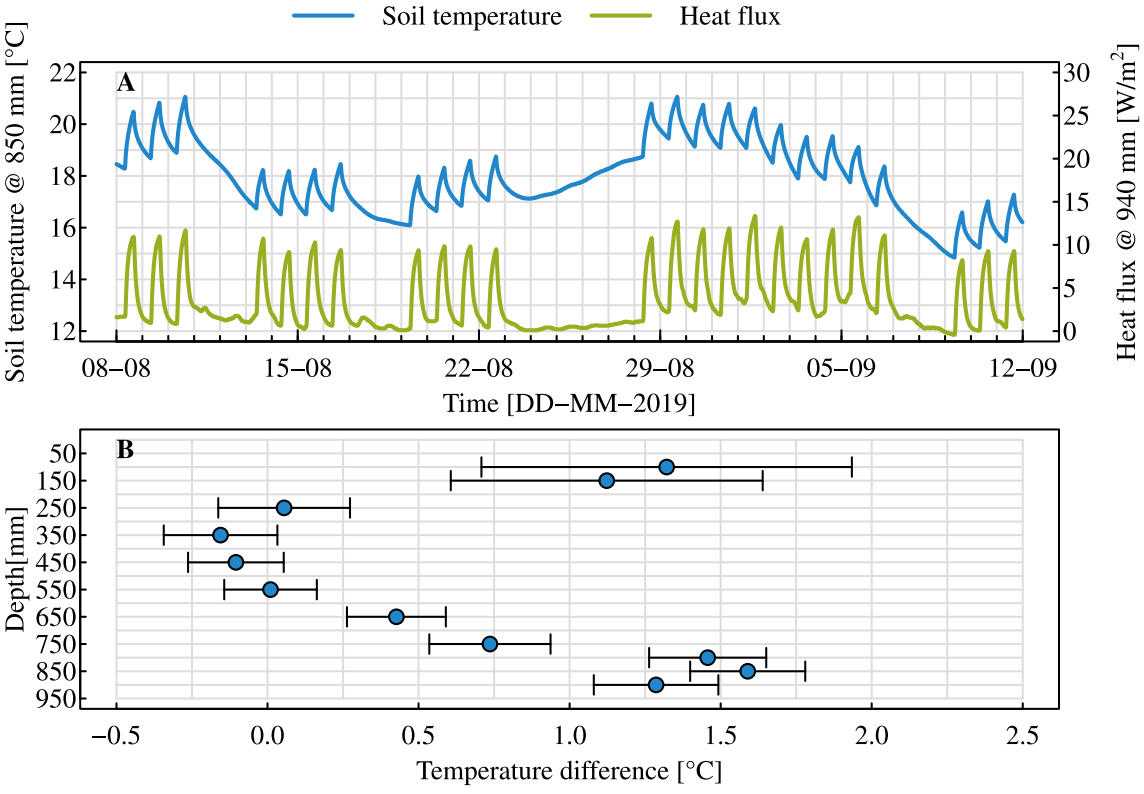

Fig. 7. (A) Soil temperature measured around heating cable at 850 mm and heat flux at 940 mm, (B) difference between the soil temperature at the start and at the end of each test in Set II. Error bars in (B) show the standard deviation.

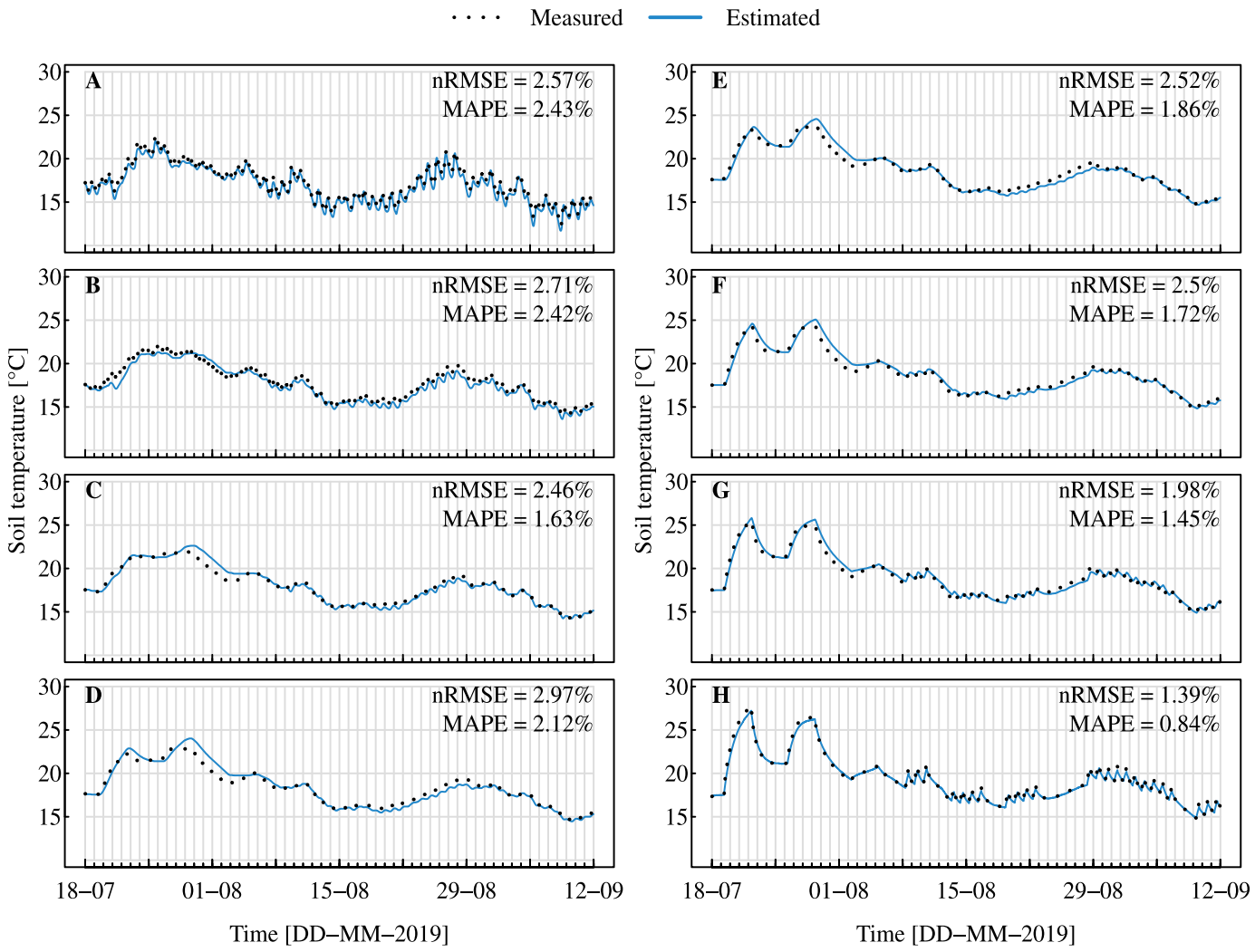

Fig. 8. Measured and estimated soil temperature data at (A) 100, (B) 250, (C) 350, (D) 450, (E) 550, (F) 650, (G) 750 and (H) 850 mm. Values in the subfigures present normalised root mean square error (nRMSE) and mean absolute percentage error (MAPE).

4.1.3. Heat injection tests

The first set of the heat injection tests took place between 19.07.2019 08:30 and 05.08.2019 08:30. Each test lasts 72 h, and there is 96-h off period in between the tests. Fig. 6a shows the soil and air temperature during Set I, while Fig. 6b presents the heat flux measured at the bottom of the soil column for the same period.

The maximum increase in soil temperature can be seen from the measurements in the immediate vicinity of the heating cable at 850 mm. Initial temperatures at 850 mm in the first 15 min of heat injection were recorded as 17.9, 21.4, 19.1 °C, whereas the final temperatures in the last 15 min were 27.8, 26.5, 20.9 °C for tests I-1, I-2 and I-3, respectively. Change in temperature for each test in the vicinity of the cable can be calculated as 9.9, 5.1 and 1.8 °C.

The second set covers a period between 08.08.2019 08:00 and 12.09.2019 16:00. There are 24 individual experiments conducted at a power of 30 W, which lasted between 08:00 and 16:00 of the day. Test II-4 on 13.08.2019 started at 09:30 due to a power failure. Exact timing of each experiment can be found in Table 2.

Fig. 7a illustrates the soil temperature around the heating cable as well as the heat flux measured at the bottom of the soil column. Each experiment shows a non-linear increase of soil temperature with time until a maximum value is reached at the end of each simulated heat injection test. Heat flux shows the same trend as the soil temperature. Peak heat flux coincides with the maximum temperature observed in each test. Even though the power applied to the heating cable was consistent for all the experiments in Set II, the maximum heat flux varied between 8.2 and 13.4 W/m^2. The maximum and minimum soil temperature measured around the heating cable ranged between 16.6–21.1 °C and 14.8–19.4 °C, respectively. Fig. 7b shows the difference between the soil temperature at the start and end of each test in Set II recorded at multiple locations in the soil column. A high variation can be seen close to the surface due to air temperature fluctuation and around the heating cable due to heat injection. Mean temperature differences are positive at the shallow layers and around the heating cable, whereas it approaches to 0 at the mid-section of the column.

4.2. Numerical modelling

R scripts developed for the numerical modelling as well as the estimated soil temperature data have been made available for public access in Yildiz and Stirling (2022b). The initial condition is defined as the beginning of the monitoring period presented herein, i.e. 18.07.2019 00:00.

Fig. 8 illustrates the results of the model calculation and measured data. The simulation is able to capture fluctuation in the temperature throughout the soil column. There is a slight overestimation of peak temperatures in the deeper layers during Set I of the heat injection tests (see Fig. 8f–h), which is not present during Set II. Temperatures in the shallow layers are underestimated throughout the monitoring period (see Fig. 8a–d). Coefficients of determination, R^2, of the measured and

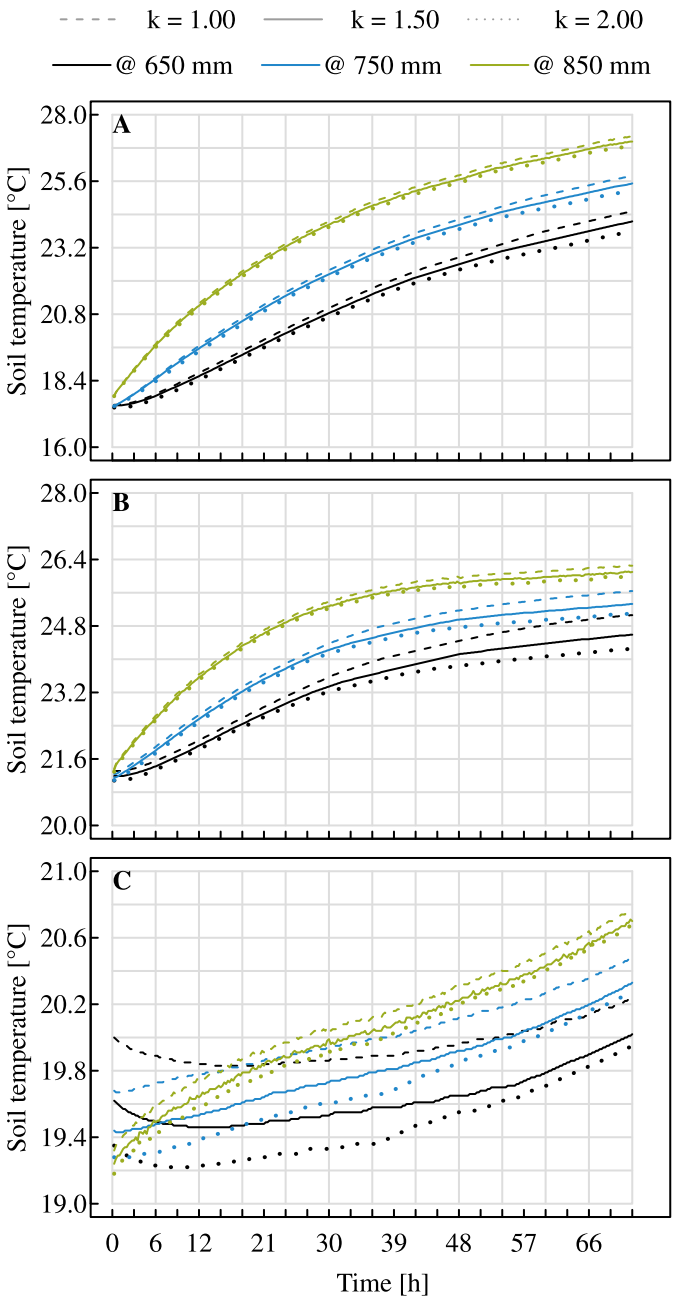

Fig. 9. Simulated soil temperature under for the field tests (A) Test I-1, (B) Test I-2 and (C) Test I-3 simulated with hydrological multiplication factors (k) of 1.00, 1.50 and 2.00.

estimated temperatures have been calculated for each depth, which ranged between 0.92 and 0.99. The highest R^2 was obtained for the estimation of temperature at the heating cable, whereas the lowest value was observed for temperatures at the interface. Fig. 8 also presents the normalised root mean square error (nRMSE) and the mean absolute percentage error (MAPE) of the estimations. Variation of nRMSE and MAPE were similar to that of R^2.

5. Discussion

GSHP systems work in the cooling mode mostly in Summer to inject heat into the soil. The first set of the field tests was conducted in July and August 2019, which had relatively high temperatures, with exceedance probabilities of 2.9 and 5.8%, respectively, for Newcastle upon Tyne. Variable power inputs were used in this set, and an overall increase of temperature in the soil column is evident during heat injection. The changes in the soil temperature around the heating cable, as well as in the deep layers (more than 550 mm), is a function of the power input (see Section 4.1.3).

Off periods during the first set of the field tests are characterised by an initial sharp decrease of temperature in the deep layers. Subsequent behaviour is clearly controlled by the air temperature. After Test I-1 is finished, as the air temperature is around 22 °C, the soil temperature of the column is also reaching to a plateau around the same value. However, the soil temperatures are decreasing steadily in the off period after Test I-2, as the outside is cooler than soil column.

Monitoring of temperature in the soil column under sustained heat injection (see Fig. 6) and daily heat injection (see Fig. 7) shows that the temperature increase due to heat injection from a GSHP system extends only to a certain depth. Shallow layers, less than 350 mm deep in this scenario, are affected from the diurnal and seasonal variation of air temperature. This can suggest that temperature increase due to heat injected into the soil will have limited affect on the plant performance – such as growth and development (Hatfield and Prueger, 2015), nutrient (Pregitzer and King, 2005) and water (Lv et al., 2013) uptake – of GI components, as the temperatures are still a function of atmospheric conditions in the shallow layers. However, this suggestion cannot be extended to the performance of deep-rooting plants.

Numerical modelling framework presented in this study considers the heat injection as an incoming flux from the heat exchanger, i.e. heating cable in the field setup, and a one-dimensional heat transfer. Similar models have been proposed in the literature, such as Nowamooz et al. (2015) and Chalhoub et al. (2017). Effects of varying hydrological regime under rainfall and drying are considered by defining volumetric water content dependent thermal diffusivity and volumetric heat capacity equations. The importance of considering soil–atmosphere interaction in the numerical calculations of horizontal ground heat exchangers (Tang and Nowamooz, 2020) and the influence of rainfall on their performance (Go et al., 2015) have been highlighted by many researchers. The model developed in this study does not perform the coupling of thermal and hydrological processes by solving equations of heat conduction and water infiltration simultaneously. However, coupling of these phenomena has been done indirectly by defining equations of thermal parameters as a function of volumetric water content (see Eqs. (8)–(10)) and using actual measurements of hydrological regime of the soil column as model input. Fig. 8 illustrates that the model developed can simulate both the variation and the magnitudes of soil temperature measurements in the substrate of a green infrastructure component, which is supported by high R^2 values (0.92–0.99) and low model error metrics (~2%). Given that the water content is measured in the soil column and the thermo-hydrological relationships are established, this modelling scheme was then used to perform predictive numerical experiments.

Fig. 9 illustrates how the water content is affecting the heat transfer during heat injection by presenting the simulated temperature profile during the first set of the heat injection tests. A reduction in the temperature around the heating cable and deep layers can be seen with increasing water content. A more efficient heat transfer in unsaturated soils with increasing water content or soils reaching to saturation from a dry state was also demonstrated by Gao et al. (2016, 2020) for horizontal ground heat exchangers, and Ahmad et al. (2021) for underground cables using laboratory setups.

Heat signatures resulting from both injection tests (Sets I and II) as well as a diurnal signal are clearly visible in Fig. 10. Set I manifests as higher temperature plumes with a sub-vertical orientation originating at 850 mm with the lag being a result of heat propagation emanating from the heating element. The intensity of their signal is approximately proportional to their respective power inputs. Crucially, these plumes indicate the limited extent of influence of the injected heat to 200–350 mm depth where upon the influence of the diurnal signal becomes

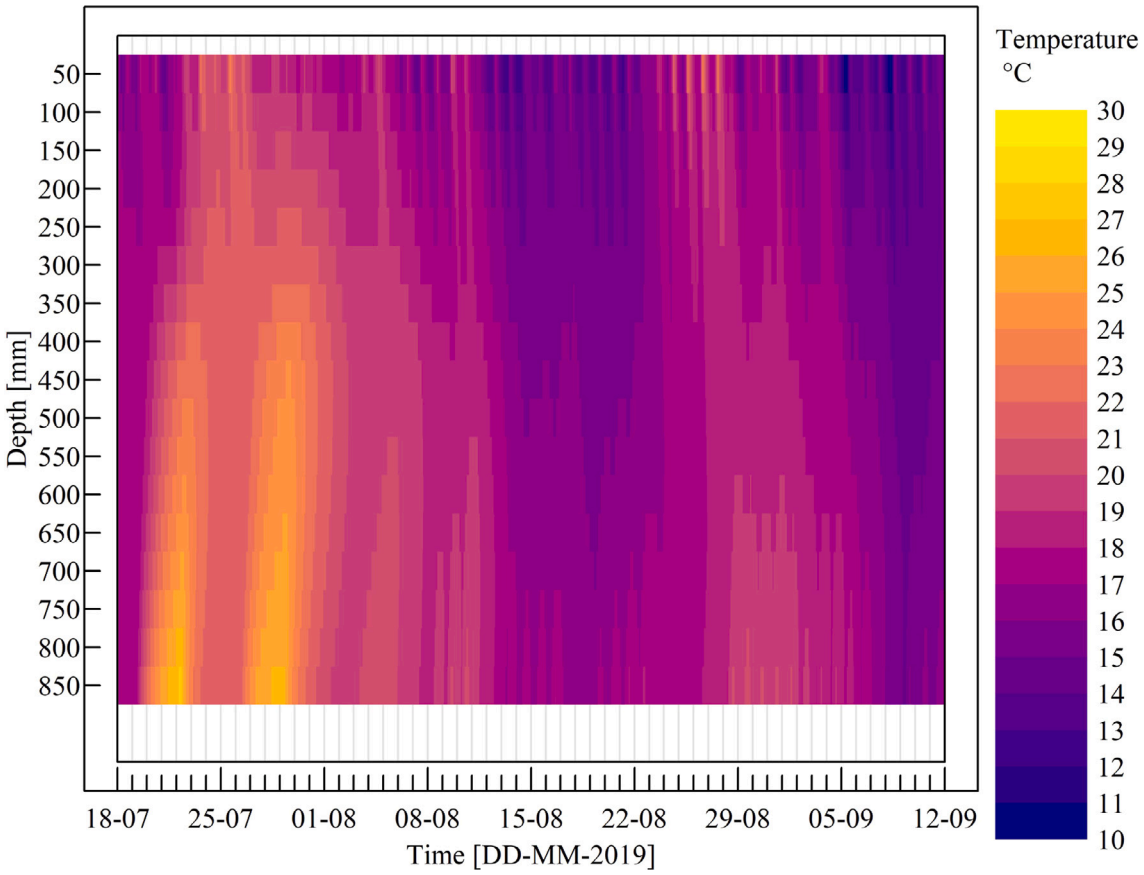

Fig. 10. Predicted soil temperatures in the field setup.

the more dominant factor. Daily air temperature fluctuations result in near-surface temperature signals that reach depths of 100–250 mm during Set I, the shallowest effect being due to a period of coincident warm soil surface temperatures and Test I-1. The diurnal signal is deeper during Set II (lower power input) and between sets. The upward extent of Set II warming is less than in Set I and a cooler period of daily surface temperatures is shown to override any warming effects of Set II, this creates a buffering zone at 350–600 mm where both upper and lower temperature inputs are effectively dampened.

This evidence suggest that a rooting zone of approximately 300–400 mm depth is largely unaffected by daily heat injection operation and that elevated temperatures which may have potentially negative effects on root activity are most likely when prolonged, relatively high power input are coincident with sustained warm weather — this highlights a need to either build in daily down-time in heat injection or if operated at reduced power, prolonged injection may be accommodated. Finally, this work has demonstrated the rapid ability of the soil temperature profile to re-equilibrate following heat injection according to the ambient surface temperature.

6. Conclusions

Potential of utilising green infrastructure as a medium for ground heat exchange has been investigated by conducting heat injection tests in a heavily-instrumented bespoke field setup. Change in soil temperature due to injected heat has been modelled with a finite difference scheme. Field monitoring shows that the increase in temperature at the vicinity of the source was a function of the power input. Shallow layers were only affected by the diurnal cycle of the air temperature, while the deeper layers were affected mainly by the heat injection. Numerical model presented in this study solves a one-dimensional heat transfer problem with finite difference model. Thermo-hydrological coupling was done by using equations of thermal parameters as a function of water content, which was substituted with actual field measurements. Model was capable of simulating heat injection into green infrastructure under various thermal scenarios. A more efficient heat transfer around the heat source with increasing water content was demonstrated by numerical experiments performed with the validated model.

Based on the empirical evidence and validated model presented, further work will explore the thermal behaviour beneath GI under a range of scenarios including seasonality and extreme hydrological loading from storm events as well as the limits of effective GSHP operation. Long-term monitoring of functional-scale GHE-SuDS would help to establish the full potential of this combined approach, including both heating and cooling modes, and would allow study into the combined effects on both systems with a more advanced numerical model.

CRediT authorship contribution statement

Anil Yildiz: Methodology, Formal analysis, Investigation, Data curation, Writing – original draft, Writing – review & editing, Visualization. **Ross A. Stirling:** Conceptualization, Methodology, Writing – review & editing, Supervision, Project administration, Funding acquisition.

Declaration of competing interest

The authors declare that they have no known competing financial interests or personal relationships that could have appeared to influence the work reported in this paper.

Data availability

Datasets related to this article can be found as a collection at doi: 10.6084/m9.figshare.c.5312786, hosted at Figshare (Yildiz and Stirling, 2022a). R scripts used in numerical modelling and visualisation can be found at doi: 10.6084/m9.figshare.17303792, hosted at Figshare (Yildiz and Stirling, 2022b). A reproducible version of this publication can be found as a Jupyter Notebook at Yildiz and Stirling (2022c), hosted at Binder.

Acknowledgements

This work was funded by the Engineering and Physical Sciences Research Council, UK (grant number EP/R013535/1) and conducted at the UKCRIC National Green Infrastructure Facility (grant number EP/R010102/1). The Authors would like to thank the following individuals for their assistance with laboratory testing and filling of the lysimeter: Fraser Storie, Gareth Wear, Michael Finley, Dr Eleanor Starkey. The Authors would also like to express their gratitude to Assoc Prof Ufuk Sahin and Dr Peter Helm for their help in model development.

References

Ahmad, S., Risvi, Z.H., Loose, J., Wuttke, F., Tirth, V., Islam, S., 2021. Temperature field around underground power cable for dry and saturated conditions under static and cyclic thermal loads. Energies 14, 8191. http://dx.doi.org/10.3390/en14238191.

Allen, R.G., Pereira, L.S., Raes, D., Smith, M., 1998. FAO Irrigation and Drainage Paper No. 56 - Crop Evapotranspiration. Technical Report, The Food and Agriculture Organization of the United Nations.

Campbell Scientific, 2021a. 107 Ttemperature probe. https://www.campbellsci.co.uk/107. Accessed: 2021-06-06.

Campbell Scientific, 2021b. CR800 measurement and control datalogger. https://www.campbellsci.co.uk/cr800. Accessed: 2021-06-06.

Campbell Scientific, 2021c. TCAV-L averaging soil thermocouple probe. https://www.campbellsci.co.uk/tcav-l. Accessed: 2021-06-06.

Chalhoub, M., Bernier, M., Coquet, Y., Philippe, M., 2017. A simple heat and moisture transfer model to predict ground temperature for shallow ground heat exchangers. Renew. Energy 103, 295–307. http://dx.doi.org/10.1016/j.renene.2016.11.027.

Chong, C.S.A., Gan, G., Verhoef, A., Garcia, R.G., Vidale, P.L., 2013. Simulation of thermal performance of horizontal slinky-loop heat exchangers for ground source heat pumps. Appl. Energy 104, 603–610. http://dx.doi.org/10.1016/j.apenergy.2012.11.069.

Dalla Santa, G., Galgaro, A., Sassi, R., Cultrera, M., Scotton, P., Mueller, J., Bertermann, D., Mendrinos, D., Pasquali, R., Perego, R., Pera, S., Di Sipio, E., Cassiani, G., De Carli, M., Bernardi, A., 2020. An updated ground thermal properties database for GSHP applications. Geothermics 85, 101758. http://dx.doi.org/10.1016/j.geothermics.2019.101758.

Day, A., Jones, P., Maidment, G., 2009. Forecasting future cooling demand in London. Energy Build. 41, 942–948. http://dx.doi.org/10.1016/j.enbuild.2009.04.001.

De Vries, D.A., 1963. Thermal properties of soils. In: van Wijk, W.R. (Ed.), Physics of Plant Environment. John Wiley & Sons, New York, pp. 210–235.

Decagon Devices, Inc., 2016. 5TE water Content, EC and temperature sensor. http://manuals.decagon.com/Retired%20and%20Discontinued/Manuals/13509_5TE_Web.pdf. Accessed: 2021-06-06.

Decagon Devices, Inc., 2017. MPS-2 & MPS-6 dielectric water potential sensors. http://manuals.decagon.com/Retired%20and%20Discontinued/Manuals/13755_MPS-2and6_Web.pdf. Accessed: 2021-06-06.

Delta-T Devices, 2021. GP2 data logger and controller. https://delta-t.co.uk/product/gp2/. Accessed: 2021-06-06.

Di Sipio, E., Bertermann, D., 2017. Factors influencing the thermal efficiency of horizontal ground heat exchangers. Energies 10, 1897. http://dx.doi.org/10.3390/en10111897.

DiCarlo, A.A., 2021. Novel seasonal enhancement of shallow ground source heat pumps. Appl. Therm. Eng. 186, 116510. http://dx.doi.org/10.1016/j.applthermaleng.2020.116510.

Fleiter, T., Herbst, A., Hirzel, S., Krail, M., Frassine, C., Aydemir, A., Elsland, R., Ragwitz, M., Rehfeldt, M., Reuter, M., Steinbach, J., Dengler, J., Köhler, B., Dinkel, A., Bonato, P., Azam, N., Kalz, D., Reitze, F., Chacon, F.A.T., Willmann, P., Maliha, S., Schön, M., Gollmer, C., Jochem, E., Fovez, G., Tuillé, F., Lescot, D., Hartner, M., Kranzl, L., Müller, A., Fothuber, S., Hiesl, A., Hummel, M., Resch, G., Aichinger, E., Fritz, S., Liebmann, L., Toleikytė, A., Reiter, U., Catenazzi, G., Jakob, M., Naegeli, C., 2017. Mapping and Analyses of the Current and Future (2020 - 2030) Heating/Cooling Fuel Deployment (Fossil/Renewables) - Work Package 1: Final Energy Consumption for the Year 2012. European Commission under contract No. ENER/C2/2014-641, URL: https://ec.europa.eu/energy/en/studies/mapping-and-analyses-current-and-future-2020-2030-heatingcooling-fuel-deployment.

Fujii, H., Nishi, K., Komaniwa, Y., Chou, N., 2012. Numerical modeling of slinky-coil horizontal ground heat exchangers. Geothermics 41, 55–62. http://dx.doi.org/10.1016/j.geothermics.2011.09.002.

Gao, Y., Dong, S., Wang, C., Chen, Y., Hu, W., 2020. Effect of thermal intensity and initial moisture content on heat and moisture transfer in unsaturated soil. Sustainable Cities Soc. 55, 102069. http://dx.doi.org/10.1016/j.scs.2020.102069.

Gao, Y., Fan, R., Li, H., Liu, R., Lin, X., Guo, H., Gao, Y., 2016. Thermal performance improvement of a horizontal ground-coupled heat exchanger by rainwater harvest. Energy Build. 110, 302–313. http://dx.doi.org/10.1016/j.enbuild.2015.10.030.

Go, G.-h., Lee, S.-r., N.V., N., Yoon, S., 2015. A new performance evaluation algorithm for horizontal GCHPs (ground coupled heat pump systems) that considers rainfall infiltration. Energy 83, 766–777. http://dx.doi.org/10.1016/j.energy.2015.02.086.

de Gracia, A., Navarro, L., Coma, J., Serrano, S., Romaní, J., Pérez, G., Cabeza, L.F., 2018. Experimental set-up for testing active and passive systems for energy savings in buildings – Lessons learnt. Renew. Sustain. Energy Rev. 82, 1014–1026. http://dx.doi.org/10.1016/j.rser.2017.09.109.

Hatfield, J.L., Prueger, J.H., 2015. Temperature extremes: Effect on plant growth and development. Weather Clim. Extremes 10, 4–10. http://dx.doi.org/10.1016/j.wace.2015.08.001, USDA Research and Programs on Extreme Events.

Healy, P.F., Ugursal, V.I., 1997. Performance and economic feasibility of ground source heat pumps in cold climate. Int. J. Energy Res. 21, 857–870. http://dx.doi.org/10.1002/(SICI)1099-114X(199708)21:10<857::AID-ER279>3.0.CO;2-1.

Hukseflux, 2021. TP01 thermal properties sensor. https://www.hukseflux.com/products/thermal-conductivity-sensors/thermal-properties-sensors/tp01-thermal-properties-sensor. Accessed: 2021-06-06.

Hukseflux, 2021a. HFP01 heat flux sensor. https://www.hukseflux.com/products/heat-flux-sensors/heat-flux-meters/hfp01-heat-flux-sensor. Accessed: 2021-06-06.

Hukseflux, 2021b. STP01 soil temperature sensor. https://www.hukseflux.com/products/heat-flux-sensors/soil-temperature-sensors/stp01-soil-temperature-sensor. Accessed: 2021-06-06.

Hwang, S., Ooka, R., Nam, Y., 2010. Evaluation of estimation method of ground properties for the ground source heat pump system. Renew. Energy 35, 2123–2130. http://dx.doi.org/10.1016/j.renene.2010.01.028.

Kim, M.-j., Lee, S.-r., Yoon, S., Go, G.-h., 2016. Thermal performance evaluation and parametric study of a horizontal ground heat exchanger. Geothermics 60, 134–143. http://dx.doi.org/10.1016/j.geothermics.2015.12.009.

Kumar, P., Druckman, A., Gallagher, J., Gatersleben, B., Allison, S., Eisenman, T.S., Hoang, U., Hama, S., Tiwari, A., Sharma, A., Abhijith, K., Adlakha, D., McNabola, A., Astell-Burt, T., Feng, X., Skeldon, A.C., de Lusignan, S., Morawska, L., 2019. The nexus between air pollution, green infrastructure and human health. Environ. Int. 133, 105181. http://dx.doi.org/10.1016/j.envint.2019.105181.

López, J., Echeverría, J., San Martín, I., Delgado, O., 2020. Dynamic testing in columns for soil heavy metal removal for a car park SUDS. Sci. Total Environ. 738, 140229. http://dx.doi.org/10.1016/j.scitotenv.2020.140229.

Lund, J.W., Boyd, T.L., 2016. Direct utilization of geothermal energy 2015 worldwide review. Geothermics 60, 66–93. http://dx.doi.org/10.1016/j.geothermics.2015.11.004.

Lv, G., Hu, W., Kang, Y., Liu, B., Li, L., Song, J., 2013. Root water uptake model considering soil temperature. J. Hydrol. Eng. 18 (4), 394–400. http://dx.doi.org/10.1061/(ASCE)HE.1943-5584.0000642.

Marando, F., Heris, M.P., Zulian, G., Udías, A., Mentaschi, L., Chrysoulakis, N., Parastatidis, D., Maes, J., 2022. Urban heat island mitigation by green infrastructure in European Functional Urban Areas. Sustainable Cities Soc. 77, 103564. http://dx.doi.org/10.1016/j.scs.2021.103564.

Naylor, S., Ellett, K.M., Gustin, A.R., 2015. Spatiotemporal variability of ground thermal properties in glacial sediments and implications for horizontal ground heat exchanger design. Renew. Energy 81, 21–30. http://dx.doi.org/10.1016/j.renene.2015.03.006.

Nowamooz, H., Nikoosokhan, S., Lin, J., Chazallon, C., 2015. Finite difference modeling of heat distribution in multilayer soils with time-spatial hydrothermal properties. Renew. Energy 76, 7–15. http://dx.doi.org/10.1016/j.renene.2014.11.008.

Ochsner, T.E., Sauer, T.J., Horton, R., 2007. Soil heat storage measurements in energy balance studies. Agron. J. 99 (1), 311–319. http://dx.doi.org/10.2134/agronj2005.0103S.

Pregitzer, K., King, J., 2005. Effects of soil temperature on nutrient uptake. In: Nutrient Acquisition by Plants. Springer-Verlag, Berlin/Heidelberg, pp. 277–310. http://dx.doi.org/10.1007/3-540-27675-0_10.

R Core Team, 2020. R: A Language and Environment for Statistical Computing. R Foundation for Statistical Computing, Vienna, Austria.

Self, S.J., Reddy, B.V., Rosen, M.A., 2013. Geothermal heat pump systems: Status review and comparison with other heating options. Appl. Energy 101, 341–348. http://dx.doi.org/10.1016/j.apenergy.2012.01.048.

Šeďová, M., Adamovský, R., Neuberger, P., 2013. Analysis of ground massif temperatures with horizontal heat exchanger. Res. Agric. Eng. 59 (3), 91–97. http://dx.doi.org/10.17221/30/2012-RAE.

Simms, R.B., Haslam, S.R., Craig, J.R., 2014. Impact of soil heterogeneity on the functioning of horizontal ground heat exchangers. Geothermics 50, 35–43. http://dx.doi.org/10.1016/j.geothermics.2013.08.007.

Tang, F., Nowamooz, H., 2020. Outlet temperatures of a slinky-type horizontal ground heat exchanger with the atmosphere-soil interaction. Renew. Energy 146, 705–718. http://dx.doi.org/10.1016/j.renene.2019.07.029.

The Met Office, 2020. UK and regional series. URL: https://www.metoffice.gov.uk/research/climate/maps-and-data/uk-and-regional-series.

Wu, R., Tinjum, J.M., Likos, W.J., 2015. Coupled thermal conductivity dryout curve and soil–water characteristic curve in modeling of shallow horizontal geothermal ground loops. Geotech. Geol. Eng. 33 (2), 193–205. http://dx.doi.org/10.1007/s10706-014-9811-2.

Yildiz, A., 2020. Estimating the full range of thermal conductivity dryout curve. Géotech. Lett. 10 (3), 419–423. http://dx.doi.org/10.1680/jgele.20.00055.

Yildiz, A., Stirling, R.A., 2020. Investigating green infrastructure as potential medium for ground heat exchangers. In: McCartney, J., Tomac, I. (Eds.), 2nd International Conference on Energy Geotechnics (ICEGT 2020), Vol. 205. EDP Sciences, p. 06013. http://dx.doi.org/10.1051/e3sconf/202020506013.

Yildiz, A., Stirling, R.A., 2021c. Thermo-hydrological behaviour of green infrastructure: A comparative field and laboratory study. Geomech. Energy Environ. 25, 100219. http://dx.doi.org/10.1016/j.gete.2020.100219.

Yildiz, A., Stirling, R.A., 2022a. PLEXUS@NGIF - Heat Injection Tests. http://dx.doi.org/10.6084/m9.figshare.c.5312786.

Yildiz, A., Stirling, R.A., 2022b. PLEXUS@NGIF - Numerical Modelling. http://dx.doi.org/10.6084/m9.figshare.17303792.

Yildiz, A., Stirling, R.A., 2022c. Yildiz & Stirling (2022) - Jupyter notebook. https://mybinder.org/v2/gh/yildizanil/ngif_heat_injection/HEAD. Accessed: 2022-01-31.